Modification of Polar Low Development by Orography and Sea Ice

DENIS SERGEEV[a] AND IAN A. RENFREW

School of Environmental Sciences, University of East Anglia, Norwich, United Kingdom

THOMAS SPENGLER

Geophysical Institute, University of Bergen, and Bjerknes Centre for Climate Research, Bergen, Norway

(Manuscript received 7 March 2018, in final form 15 June 2018)

ABSTRACT

The life cycles of intense high-latitude mesoscale cyclones and polar lows are strongly shaped by their ambient environments. This study focuses on the influence of the orography of Svalbard and the sea ice cover in the Norwegian and Barents Seas on polar low development. We investigate two typical polar lows that formed near Svalbard during northerly cold-air outbreaks. Each case is simulated using the Met Office Unified Model with convection-permitting grid spacing. A series of sensitivity experiments is conducted with an artificially changed land mask, orography, and sea ice distribution. We find that Svalbard acts to block stably stratified air from the ice-covered Arctic Ocean, and as an additional source of low-level cyclonic vorticity aiding polar low genesis and intensification. A decrease in sea ice cover west of Svalbard results in a moderate intensification of the polar lows, particularly for the more convectively driven case, while an increase in the sea ice cover significantly hinders their development. These experiments exemplify that polar mesoscale cyclones in the northeast Atlantic can withstand large perturbations in the surface conditions (such as the removal of Svalbard) and still develop to sufficient intensity to be labeled as polar lows. However, there is a sensitivity to Svalbard's orography and surrounding sea ice cover, illustrated by a clear modulation of polar low genesis and development.

1. Introduction

High-latitude mesoscale cyclones, and their intense subcategory polar lows (PLs), usually occur concomitantly with marine cold air outbreaks (CAOs) (e.g., see Kolstad 2006). The Svalbard Archipelago is the major orographic obstacle for these CAOs in the Norwegian and Barents Seas and climatological studies (e.g., Condron et al. 2006; Michel et al. 2018) report a maximum of mesoscale cyclone activity in its vicinity. With a retreating Arctic sea ice (Cavalieri and Parkinson 2012), PL activity is predicted to move mainly northward (Zahn and Von Storch 2010) and northeastward (Romero and Emanuel 2017); although Michel et al. (2018) suggest that no significant correlation between PL activity and sea ice extent in the North Atlantic has been observed so far. This controversy calls for more investigation of the mechanisms of cyclone interactions with the surface. In this paper, we present a high-resolution modeling study of two PL events in the Norwegian Sea and examine their sensitivity to Svalbard's orography and the sea ice distribution around it.

Orographic barriers generate flow distortions that may evolve into PLs in high latitudes (Rasmussen 1981). In general, the potential impact of orography on the atmospheric flow is dependent on the wind speed and the stability of the atmosphere as well as the size and shape of the barrier. These parameters are encapsulated by the nondimensional mountain height and the horizontal mountain aspect ratio (Smith 1989a). Depending on these criteria, the flow over mountains can affect cyclogenesis via upstream blocking, flow splitting, and lee vorticity stretching.

Low-level flow blocking by an elongated mountain can hold back the flow creating more favorable conditions for mesoscale cyclone growth downstream. For example, Watanabe et al. (2017) found that the mountain

Denotes content that is immediately available upon publication as open access.

[a] Current affiliation: College of Engineering, Mathematics, and Physical Sciences, University of Exeter, Exeter, United Kingdom.

Corresponding author: D. E. Sergeev, d.sergeev@exeter.ac.uk

DOI: 10.1175/MWR-D-18-0086.1

ridge on the northern coast of the Sea of Japan blocks dry and stably stratified air from Eurasia; in simulations without these mountains, the continental CAO sweeps mesoscale cyclones closer to Japan, leaving less opportunity to gain energy over the warm sea, leading to landfall prior to full development. Although the highest peak of Svalbard is only 1717 m, the flow distortion associated with the archipelago is comparable to that of far higher mountains because of the climatologically high static stability (Skeie and Gronas 2000).

Lee cyclogenesis has been reported to produce mesoscale lows in the North Atlantic (Petersen et al. 2003), the Sea of Japan (Watanabe et al. 2018), and the Ross Sea (Gallée 1995). Via a series of sensitivity experiments, Kristjánsson et al. (2011) show that the orography of eastern Greenland can lead to a spinup of low-level circulation that develops into an intense PL over the Denmark Strait. The subsidence associated with vortex stretching and adiabatic warming is absent without Greenland. On a smaller scale, lee vorticity production can be invigorated by katabatic winds, as shown by Gallée (1995) for the Antarctic Peninsula. Katabatic convergence in the wake of Greenland can also be conducive for the formation of mesoscale cyclones (Klein and Heinemann 2002). Similar effects have not been investigated around Svalbard.

The flow deflection by a mountain with sufficient nondimensional height can produce low-level jets at its flanks, referred to as "tip jets" (Doyle and Shapiro 1999; Renfrew et al. 2009; Outten et al. 2009). They regularly appear near the southernmost point of Greenland (Moore and Renfrew 2005). Tip jet formation has also been observed at the southern cape of Spitsbergen, the largest island of the Svalbard Archipelago (Reeve and Kolstad 2011). The shear vorticity associated with such jets can create a conducive environment for barotropic instability (Skeie and Gronas 2000), potentially leading to cyclogenesis. However, a link between the flow distortion caused by Svalbard and local PL activity remains unclear (Bracegirdle and Gray 2008). To our knowledge, there has been scarcely any research focused on the mechanisms by which such flow responses to orography may contribute to the development of PLs. Thus, the first question we address here is *to what degree does the presence of Svalbard affect PL formation and spinup*.

PLs are also sensitive to the sea ice and sea surface temperature (SST), via their influence on low-level baroclinicity and surface heat fluxes. The sea ice edge represents a zone with sharp gradients of temperature and albedo, resulting in shallow baroclinic zones that can spawn mesoscale vortices (e.g., Harold et al. 1999). In addition, differences in surface roughness between the open water and the ice can result in shear vorticity generation and consequently barotropic cyclogenesis (Rasmussen and Turner 2003).

The shape of the sea ice edge is important in the formation of a downstream convergence zone that can be favorable for PL generation. This mechanism of mesoscale cyclone development was addressed by Heinemann (1997) in idealized numerical simulations of Weddell Sea vortices. Because of the differential heating in that region, pressure fell in a belt parallel to the sea ice edge, forming a meso-β-scale (about 200 km in diameter) circulation. In Albright et al. (1995) the intensity and location of a PL in Hudson Bay was found to be strongly dependent on the upstream sea ice edge. The sea ice edge in the Svalbard region has a concave shape forming a bay of open water to the west of the archipelago, which is potentially conducive to convergence within CAOs, and this could influence mesoscale cyclone generation.

Turbulent heat fluxes over the sea ice are too small for PL intensification, whereas over the ice-free ocean they can create a favorable environment for PLs by destabilizing the atmosphere. To reproduce a baroclinic PL moving northeastward, Adakudlu and Barstad (2011) modified the SST and sea ice cover over the Barents Sea. Their removal of sea ice allowed the simulated PL to develop and persist for longer than in a control case. In addition, increased SST led to a strong vertical coupling between the PL and an upper-level potential vorticity (PV) anomaly. A recent study by Watanabe et al. (2017) also demonstrates that the sea ice configuration in the Sea of Japan and the Strait of Tartary is conducive to the development of mesoscale vortices. In a sensitivity experiment with increased sea ice cover and reduced SST the fluxes from the surface are limited resulting in a more stably stratified atmosphere, reducing the influence of upper-level forcing. In the context of the Nordic Seas, we address the following second question: *what influence does the sea ice extent near Svalbard have on PLs?*

2. Data and methodology

a. Polar low cases

To find suitable cases, we perused the Sea Surface Temperature and Altimeter Synergy for Improved Forecasting of Polar Lows (STARS) database, which is freely available to the community (http://polarlow.met.no). It contains a total of 140 PL tracks in the northeast Atlantic for the period 2002–11. After manual inspection of the cloud imagery and PL tracks, a dozen candidates were chosen based on their proximity to Svalbard and general southward propagation. These criteria imply that we are interested in PLs that originate immediately downstream of the archipelago in the airstreams coming from the sea ice. Following preliminary simulations of all of these cases, here we

present two cases that are illustrative of the range of PL examined: the 5–6 April 2007 (STARS-72) and the 30–31 January 2008 (STARS-77).

These two cyclones are well reproduced by the numerical model and have well-defined circulations that facilitate their tracking and clarify the analysis of sensitivity experiments. Both PLs developed in a classic northerly CAO (Papritz and Spengler 2017) and spawned very close to Svalbard, raising the possibility of its importance in their development. The two cases are somewhat different in terms of dynamical forcing, as discussed later.

b. The Met Office Unified Model

We use one of the latest versions (vn10.2) of the Met Office's Unified Model (MetUM) in atmosphere-only mode. The MetUM has been used in previous PL investigations (e.g., Bracegirdle and Gray 2009) and this particular version and configuration (Table 1) has been validated against aircraft and satellite observations of a shear-line PL by Sergeev et al. (2017). The basic equations of the model are described in Wood et al. (2014) and essentially represent the atmosphere as a deep nonhydrostatic fully compressible fluid. We use the ''ENDGame'' configuration, which incorporates significant improvements to the numerical schemes and physical parameterizations, such as a new orographic drag scheme, a corrected convection entrainment scheme, and revised turbulent mixing for shear-dominated boundary layers. The model calculates surface fluxes separately on each tile using similarity theory [details can be found in Walters et al. (2017)]. For the boundary layer, the scheme described by Brown et al. (2008) is used. Although the sensitivity of PLs to the subgrid mixing parameterization is beyond the scope of this paper, the MetUM schemes used in the present study have been tested in PL cases by Irvine et al. (2011) and Sergeev et al. (2017), who have shown that the boundary layer and surface fluxes parameterizations are suitable for reproducing these events.

A global MetUM simulation with N768 resolution (17 km) is initialized using the operational analysis and run to provide boundary conditions for the nested simulations (e.g., see Fig. 1). The horizontal grid spacing of the limited-area model is ≈2.2 km, while the time step is 60 s. Sea ice extent and SST are derived from the Operational Sea Surface Temperature and Sea Ice Analysis (OSTIA) at 17-km resolution and bilinearly interpolated to the nested model resolution. The elevation is taken from the Global Land One kilometer Base Elevation (GLOBE) dataset (Webster et al. 2003) with a grid spacing of 1 km.

The frequency of the model output is set to 1 h. Three-dimensional fields are analyzed on isobaric surfaces (29 equally spaced levels spanning 1000–300 hPa). The code used in this study relies on the iris Python package (Met Office 2016) and is available on GitHub (https://github.com/dennissergeev/mplosi). Model output data are available upon request.

TABLE 1. MetUM settings.

Version; nesting suite ID	10.2; u-ae616
Horizontal grid spacing	2.2 km
Nested domain size (x, y)	600 × 700 grid points
Rim width (grid points)	24
Nested domain area	1320 km × 1540 km
Initialization time	
STARS-72	1200 UTC 4 Apr 2007
STARS-77	1200 UTC 29 Jan 2008
Run duration	48 h
Output frequency	1 h

c. Trajectory analysis

To investigate how the PLs form and obtain their warm cores, we calculate kinematic trajectories backward in time, applying the Lagrangian Analysis Tool (LAGRANTO), version 2.0 (Sprenger and Wernli 2015), to the MetUM output of the three wind components and sea level pressure. Similar trajectory analysis of PLs over the Sea of Japan has been carried out by Watanabe and Niino (2014) and Watanabe et al. (2017), and has been proven to be useful for CAO climatology work by Papritz and Spengler (2017) as well as for the mesoscale flow interaction with topography in polar regions by Elvidge et al. (2015). Trajectories from five pressure levels (950, 925, 900, 875, and 850 hPa) over a 10 km × 10 km grid within the warm core of the PLs are calculated backward in time for 24 h from the time of maximum intensity (defined as the time when the PL reaches its maximum relative vorticity in the lower troposphere).

d. Experimental setup

We start with control (CTRL) experiments for each of the two PL cases. The model domain spans most of the Norwegian and parts of the Greenland and Barents Seas (Fig. 1). The Svalbard Archipelago is near the center of the domain. The surface temperature and sea ice cover are similar in both PL cases; namely, a ''diagonally oriented'' sea ice edge in Fram Strait, a bay of open water to the west of Svalbard, and sea ice to the east of the archipelago.

For each case we perform four additional model simulations, where we separately change the orography and sea ice edge positions. Note that *simultaneous* changes of orography and sea ice resulted in even larger differences between the CTRL and perturbed experiments. However, the combined perturbed orography and sea ice experiments do not

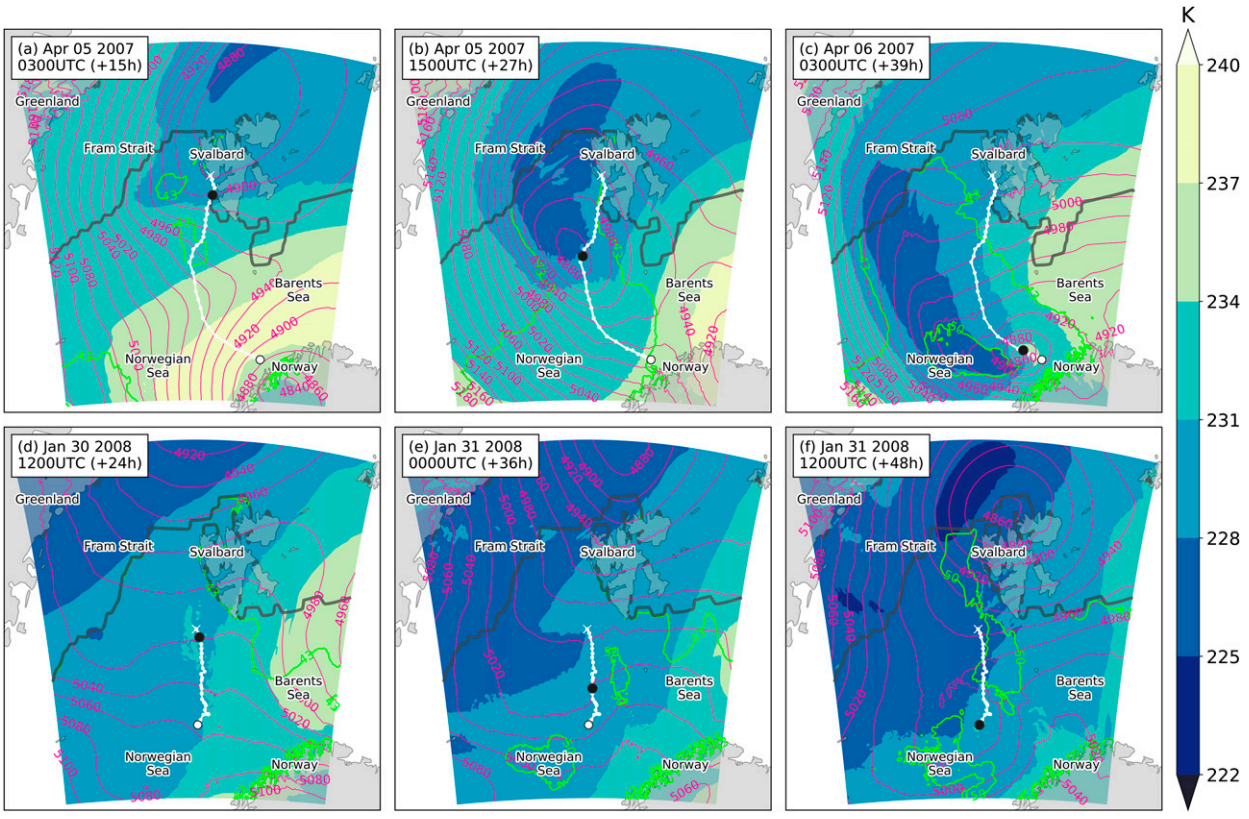

FIG. 1. The model domain showing upper-level (500 hPa) conditions for the (a)–(c) STARS-72 case and (d)–(f) STARS-77 case. Shown are air temperature (color shading, K), geopotential height (pink contours, m), SST − T_{500} (selected for 43- and 50-K isotherms, green), and the sea ice edge (dark gray line). The PL tracks are marked in white, a white cross showing the start, and black and white dots showing the PL location at the time of the panel and after 48 h, respectively.

provide new information beyond the uncombined experiments presented here, so for the sake of brevity, these are not discussed further.

Some additional experiments were carried out to test the MetUM's sensitivity to the initialization time, the size of the model domain, and its geographical position. In the first few hours of all experiments (CTRL and sensitivity) low-level vorticity features were indistinguishable. A few weak vorticity filaments are present at the beginning of the forecast, but they dissipate or are advected away from the region of future PL formation. Thus, we believe the initialization time of the experiments is appropriate to capture the full life cycle of PLs and is not too early to render the forecast inaccurate compared to observations. Overall, the model produced very similar results even if the domain was twice as large or shifted by a few degrees latitude or longitude. Runs with doubled grid spacing (4.0 km) generally agreed with the control runs, but did not reproduce the same amount of small convective cells. These differences in the representation of discrete convective cells do not accompany significant differences in the wind and temperature fields, as was found for a higher-resolution (0.5-km grid size) simulation by Sergeev et al. (2017).

3. Results

a. *Large-scale atmospheric conditions and PL evolution in the CTRL experiments*

The surface environment prior to the PLs generation is similar in both cases. It is characterized by a quasi-zonal pressure gradient over the Norwegian Sea, on the western periphery of a synoptic-scale cyclone moving to the northeast, while a high pressure system is located over Greenland. This setting is a classic example of favorable conditions for CAOs in this area (Papritz and Spengler 2017). Accordingly, the prevailing wind direction throughout the simulation is from the north. These synoptic conditions fall into the category of the Atlantic ridge weather regime, which is found by Mallet et al. (2013) to be the most conducive for PL activity over the northeast Atlantic.

The upper-level conditions (Fig. 1) display a southward propagation of the Arctic air mass, but the geopotential height and temperature patterns differ between

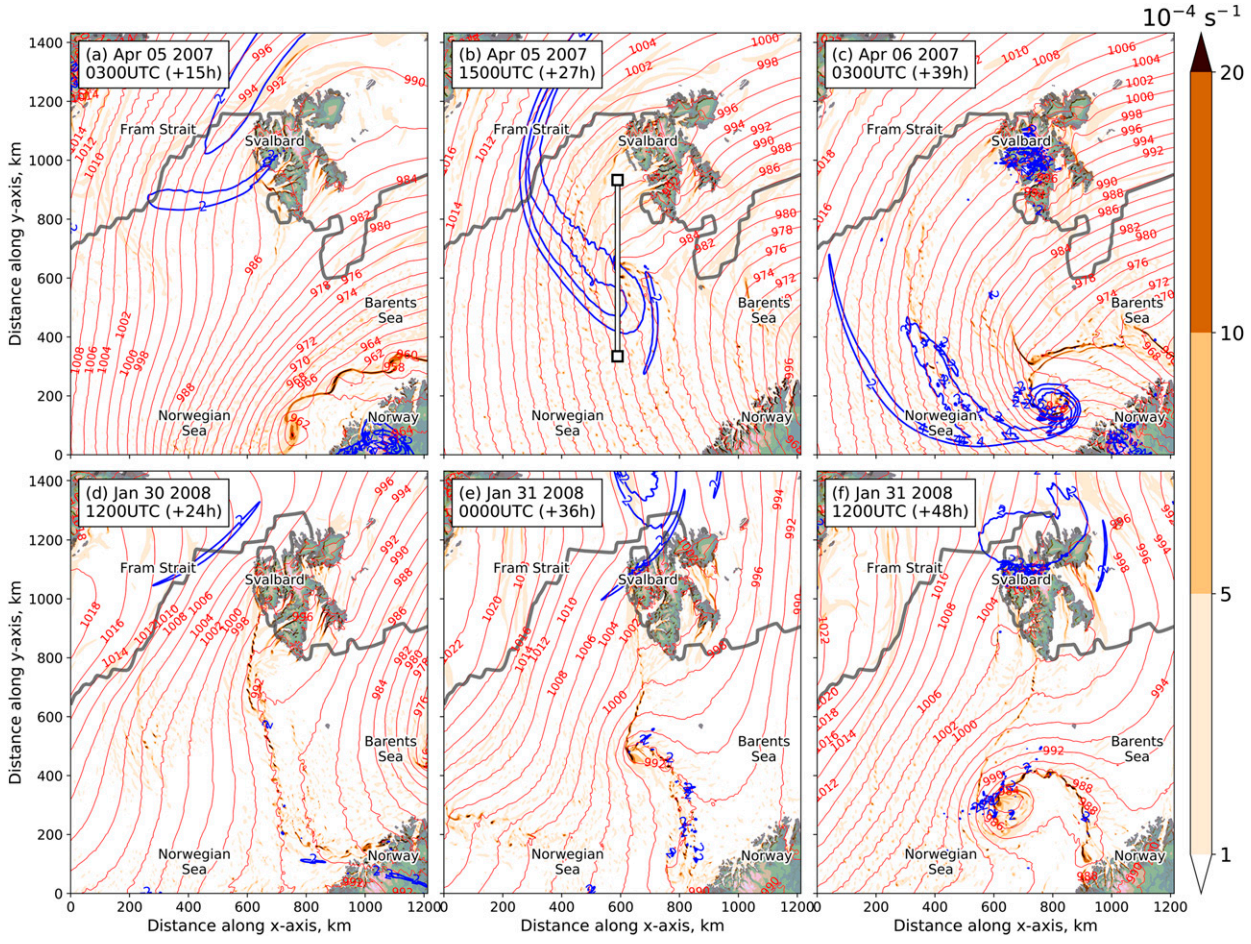

FIG. 2. As in Fig. 1, but for potential vorticity at 500 hPa (blue contours, every 2 PVU), relative vorticity at 950 hPa (color shading, 10^{-4} s^{-1}), and sea level pressure (red contours, every 2 hPa). The white line in (b) indicates the south–north vertical cross section shown in Fig. 11. Model elevation is shown by color shading.

the STARS-72 and STARS-77 cases. In the former case, a distinct cold trough at 500 hPa forms over the Svalbard region. During the PL event, this upper-level vortex becomes more concentrated and propagates toward the Scandinavian coast, elongating the cold anomaly over the western Norwegian Sea. This is reflected in the 500-hPa PV field (Fig. 2a), which contains an elongated maximum that moves to the region from the north. The moment when the forefront of the PV maximum happens to pass over Svalbard (Fig. 2a), an embryo of the future STARS-72 PL detaches from the western coast of the archipelago (evident in low-level vorticity). As the PV filament extends southward, the sea level pressure (SLP) trough and the low-level vorticity maximum associated with the growing PL follow it. The upper- and the lower-level PV anomalies (qualitatively similar to the low-level vorticity in Fig. 2) quickly become vertically aligned, with the surface PV maxima associated with convective mesoscale vortices extending up to 500 hPa (Figs. 1c and 2c). The reduction of the distance between upper- and lower-level lows, or in other words, the decrease of the baroclinic mode phase tilt in the STARS-72 case, resembles a type-B cyclogenesis in the classification of Petterssen and Smebye (Bracegirdle and Gray 2009).

The STARS-77 PL's upper-level environment, on the other hand, does not possess a well-defined cold vortex, nor does it have a strong PV anomaly. The geopotential height contours at 500 hPa remain largely zonal during the life cycle of the PL (Figs. 1d,e). A small upper-level trough appears above the PL at the end of the simulation because of the intensification of the surface mesoscale cyclone (Fig. 1f). The 500-hPa temperature field is as cold as in the first case, though the temperature minimum is less pronounced. The broad negative temperature anomaly in the midtroposphere combined with slightly higher SST in the STARS-77 case indicates that the atmosphere is less stable, compared to the first case's environment, and thus more prone to convection.

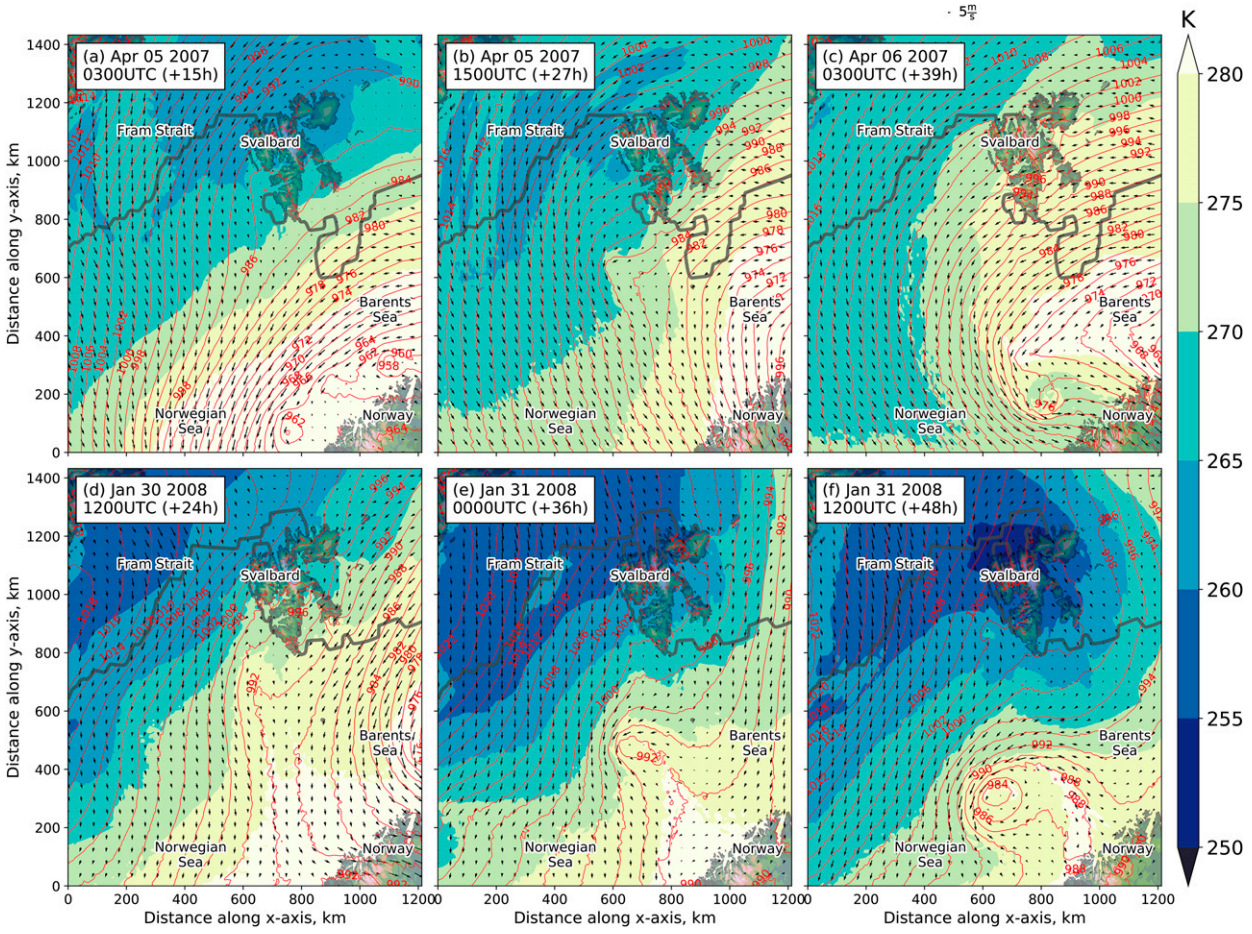

FIG. 3. As in Fig. 2, but for equivalent potential temperature (color shading, every 5 K) and horizontal wind at 850 hPa (black vectors), and sea level pressure (red contours, every 2 hPa).

This difference is more pronounced in the first day of the simulations and is demonstrated by the SST and the temperature at 500 hPa difference (SST − T_{500}, Figs. 1a,d)—a proxy often used for potential PL development (Kolstad 2011).

The low-level evolution of the STARS-77 PL begins with a series of high-vorticity banners emanating from the west coast of Spitsbergen and growing over the ice-free ocean, before merging into a long (up to ≈500 km) convergence line accompanied by a weak SLP trough (Fig. 2e and vectors in Fig. 3e). Because of a greater low-level convergence (not shown), stretching of the existing cyclonic vorticity intensifies the northern segment of the shear line quicker than its southern segment. Consequently, under the influence of northerly flow from Fram Strait and northeasterly flow from the Barents Sea, the vorticity line curls up into a comma-shaped PL (Figs. 2e,f). The barotropic nature of this wave is evident from the high horizontal gradients in the wind speed (not shown) and the characteristic scale of the vorticity waves, roughly equal to 25–30 km. Given the sharp vorticity gradient across this narrow (<20 km across) vorticity strip, Rayleigh's inflection point criterion for instability is satisfied [i.e., a maximum in vorticity is within the domain (e.g., Dritschel et al. 1991)]. The barotropic wave growth is likely to be aided by latent heat release in the banded convection (Joly and Thorpe 1990). This is related to the mechanisms examined in the idealized model experiments of Dacre and Gray (2006). This PL's high-vorticity core continues to expand, becoming more spiraliform in a similar fashion to that described by Schär and Davies (1990), while the central pressure drops below 984 hPa at the end of the simulation (Fig. 2f).

Both PLs develop in a similar ambient horizontal equivalent potential temperature gradient of roughly 1.5 K $(100\,\text{km})^{-1}$ in the lower troposphere (Fig. 3). The incipient mesoscale cyclones appear in the northern part of the baroclinic zone that stretches from southwest to northeast (Figs. 3a,d). The warm air mass and the

large-scale surface low retreat to the east and are replaced by colder air brought by the CAO. The PLs develop on the eastern edge of this CAO. Toward the end of the PL life cycle, the cold air encircles warmer air, resulting in a warm seclusion in the STARS-72 case (Fig. 3c). The temperature stratification of the background environment is stronger in the STARS-72 case, than in the STARS-77 case. For example, the SST–500 hPa difference at the early stages of PL development exceeds 47 K in the STARS-77 case, which is 7 K larger than in the STARS-72 case (Fig. 1). The difference in stratification is mainly due to the mid- and upper levels being colder in the STARS-77 case (cf. Figs. 1a and 1d). This suggests a greater role of convection and diabatic destabilization in the STARS-77 case. The latter can represent a sufficient mechanism for PL intensification in the regions with sustained surface baroclinicity (Montgomery and Farrell 1992). Thus, the formation and growth of both PLs involves a synergy among baroclinic instability, convection, barotropic instability (for STARS-77), and upper-level forcing (for STARS-72).

The simulated top-of-the-atmosphere outgoing longwave radiation plots (TOA OLR; see Fig. 4) are broadly consistent with AVHRR satellite images (http://polarlow.met.no). They depict a cloud-free eye surrounded by the highest spiraling cloud bands (white shading—lowest values of TOA OLR), with precipitation rates reaching 10 mm h^{-1}. The rest of the model domain is filled by swaths of stratocumulus clouds and convective cells or cloud streets of shallow convection typical of a CAO event.

Backward trajectory analysis shows that in both cases, more than half of the air parcels that end up in the PL center originate from Fram Strait and to the north of Svalbard, as far as Franz Josef Land (pink lines in Figs. 5a and 5e). Their typical path goes over the ice-covered Fram Strait, bypassing Svalbard to the west, and moving in a southeastward direction to end up in the PL. The trajectories stay below 850 hPa (in the STARS-72 case even lower) and barely change their potential temperature θ, until about −18 h when they enter the ice-free area. Accordingly, the air parcels' temperature and, a bit later, specific humidity begin to rise because of the strong surface heat fluxes.

The highest θ in the PL core is associated with trajectories that have the western Barents Sea as their predominant origin (yellow lines in Figs. 5a and 5e). Being already much warmer than the parcels from the north, θ along trajectories from the Barents Sea increases farther as a result of diabatic processes (Figs. 5c,g, inset axes). Moisture brought by these parcels to the PL (Figs. 5d,h) helps to drive convection that is manifested by the upward movement at the end of the trajectories (e.g., Fig. 5f).

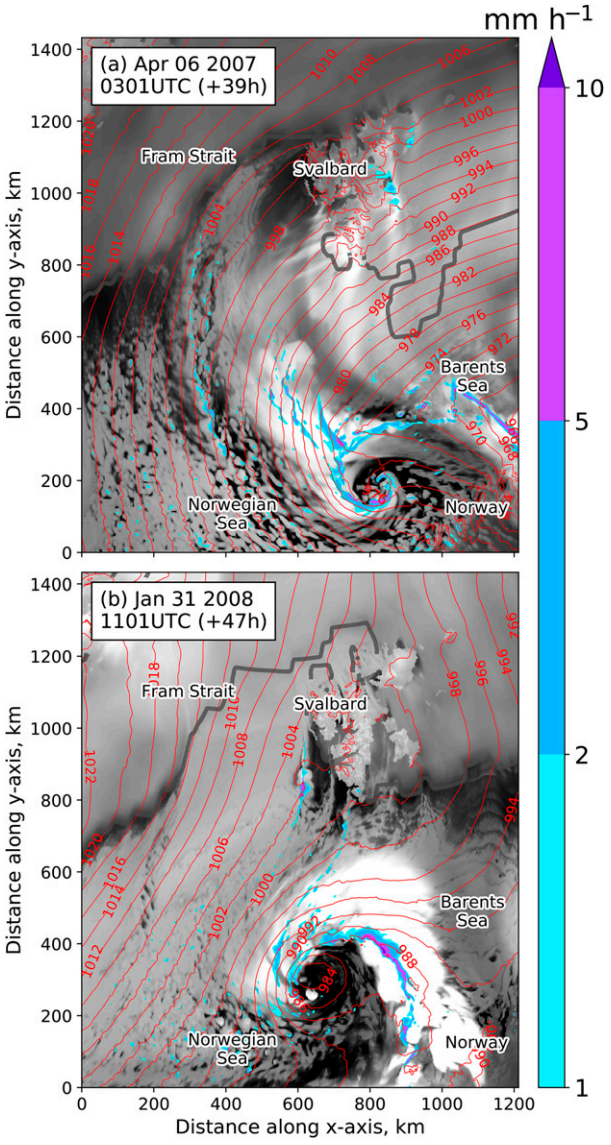

FIG. 4. Simulated cloud signature (shown by TOA OLR), SLP (red contours, hPa), and precipitation rate (mm h^{-1}) at the time of maximum intensity in case (a) STARS-72 and (b) STARS-77. The sea ice edge is shown as 15% contour line of sea ice fraction (gray line).

The STARS-77 case has an additional source of air that is located over the Greenland Sea and carried to the PL by westerlies at ≈600 hPa and higher (cyan lines in Fig. 5e). This dry air from the mid- and upper troposphere contributes to the warm core of the PL, through adiabatic warming during descent (cyan curve in the inset axes of Fig. 5g showing nearly constant θ values). The change in temperature along these trajectories is the largest of all the trajectory paths.

b. *Sensitivity experiments*

When Svalbard obstructs a CAO, it can act as a source of low-level vorticity conducive to the formation of

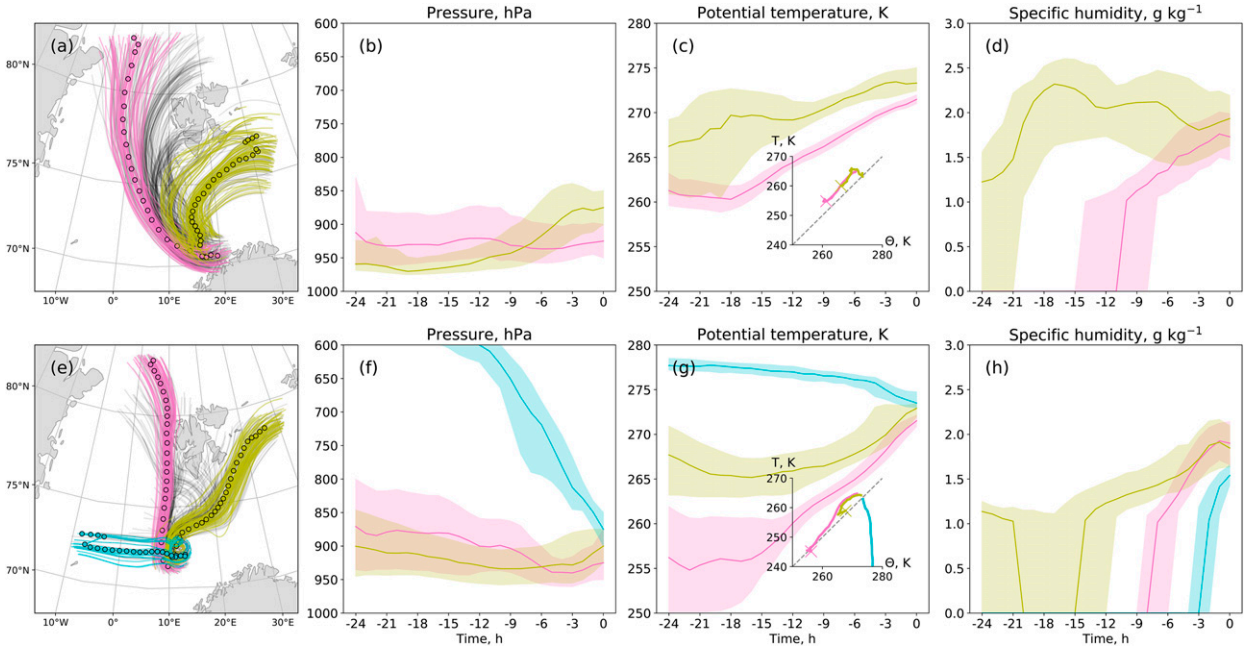

FIG. 5. Backward trajectories (a),(e) over 24 h, and time series of (b),(f) pressure; (c),(g) potential temperature; and (d),(h) specific humidity along the trajectories for the cases (top) STARS-72 and (bottom) STARS-77. Trajectories with distinct geographical origins are highlighted: north (pink), northeast (yellow), and west (cyan). Gray lines depict trajectories that do not decidedly fall into any geographical category. The colored circles show hourly positions of the air parcels along the median trajectory. The time series plots (b)–(d), (f)–(h) show the median and the interquartile range by a solid line and shading, respectively. Inset axes in subplots (c) and (g) show the θ–T diagrams, where the first hour of the trajectory is shown by a cross. The dashed diagonal line shows 1:1 ratio of θ and T increase. Note that the geographical origins are defined by longitude–latitude boxes; even though some of the gray trajectories seem to originate in the similar area, they do not cross those boxes.

mesoscale cyclones (e.g., Fig. 2). In addition, the relatively warm ice-free sea surface to the west of the archipelago supplies the heat and moisture that contribute to PL development. The shape of the sea ice edge can also be vital for flow convergence (e.g., Gryschka et al. 2008). To examine the sensitivity of the PLs to these surface factors we performed a number of sensitivity experiments (Table 2).

The CTRL surface characteristics are illustrated in Fig. 6a. The NOSVA experiment has the area of Svalbard replaced by sea ice of the same coastal shape in order to elicit the influence of the archipelago's topography (Fig. 6b). In SVA200, Svalbard's elevation is changed by a set percentage (200%) at each grid point. Consequently the vertical profile of Svalbard becomes steeper, but the coastal shape of Svalbard remains the same.

The diagonally oriented sea ice distribution in the Fram Strait and the open water next to Svalbard (see Fig. 6a) will lead to a diagonal pattern of heating from the surface that may supply energy to the growing convergence lines. In our sensitivity experiments, we make the sea ice edge oriented zonally and shift it to 82°N, north of Svalbard (ICE82N run; Fig. 6c). Then, to isolate the influence of open water west of Svalbard, we extend the sea ice cover south to 76°N (ICE76N; Fig. 6d). In the ICE82N experiment sea ice south of 82°N is replaced by ocean with an SST of 271.35 K (seawater freezing point). Note that changing the sea ice cover also changes the baroclinicity in the area, which is an inherent part of our experimental design. The effect of this additional factor would be better answered via idealized studies in future work.

1) PERTURBED OROGRAPHY EXPERIMENTS

Although the PLs still develop in the perturbed orography conditions, their origin and tracks have changed (Fig. 7). In the NOSVA run of both PL cases, the incipient vortices still appear near the ragged western ice edge replacing Spitsbergen, but are quickly advected away from

TABLE 2. Sensitivity runs setup.

Run	Svalbard	Sea ice
NOSVA	Replaced by sea ice	Control
SVA200	Height scaled by 200%	Control
ICE82N	Control	Zonal ice edge at 82°N
ICE76N	Control	Zonal ice edge at 76°N

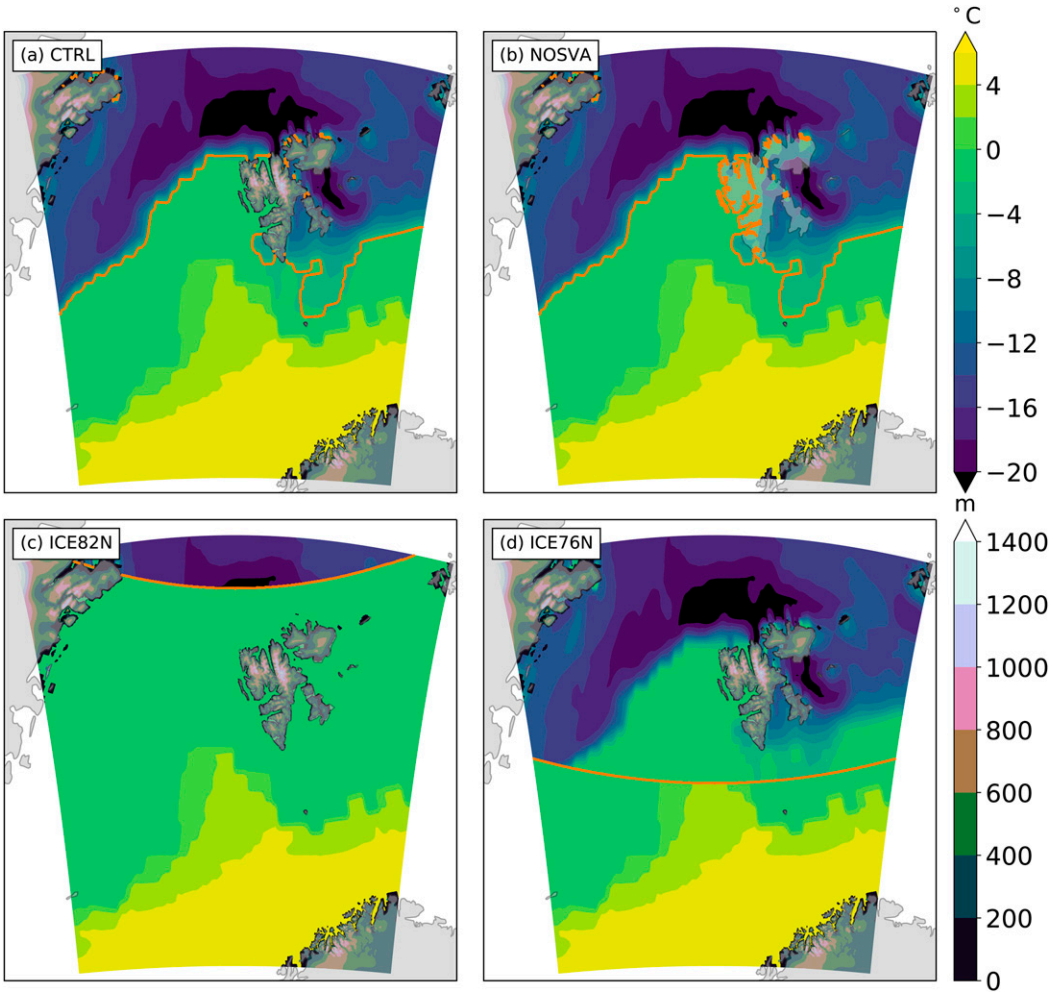

FIG. 6. Sea surface temperature (color shading, °C), surface elevation (color shading, m), and sea ice edge (orange line) in (a) CTRL, (b) NOSVA, (c) ICE82N, and (d) ICE76N simulations of the STARS-72 case.

the ice edge. As a result, they are unable to join the vorticity lines produced in a merry-go-round fashion around the synoptic-scale low to the east. The initial vorticity cluster coming from Svalbard dissipates near the Scandinavian Peninsula after about 21 h of existence. The primary nuclei of PLs in the NOSVA runs become the vortical disturbances generated by the northeasterly large-scale flow (cf. the starting locations of the PL tracks to the ones in the CTRL runs). The NOSVA PLs develop farther to the south and slightly later than CTRL PLs, likely because of the lack of vorticity reinforcement from Svalbard, illustrated in the STARS-77 case by the absence of a trailing "vorticity tail" between the archipelago and the growing PL in Fig. 7e. One can notice a remnant of the vorticity filament close to the PL, but it is detached from it and is too far west. In the STARS-77 case, the NOSVA PL is weaker than in the CTRL run when assessed by such metrics as the low-level relative vorticity averaged within 150 km of the center of the vortex (Figs. 8a,b). In the STARS-72 case, the intensity of the NOSVA PL takes more time to increase, but eventually matches the intensity of the CTRL PL.

When the height of Svalbard's mountains is doubled (SVA200 runs), the fjords produce more vorticity filaments, which feed the growing mesoscale cyclones. In both cases, intense tip jets are generated by the air flowing around the northwestern cape (not shown), consistent with the idealized experiments of Skeie and Gronas (2000) and being the major source of relative vorticity to the incipient PLs. The mesoscale cyclones are initiated closer to the archipelago because of the topographic blocking of the CAO (i.e., Svalbard acts to divert flow around it; discussed in section 4). They are characterized by a much higher vorticity at the beginning of their tracks, but comparable to the CTRL at the end. In fact, as shown in Fig. 8 the STARS-72 PL attains

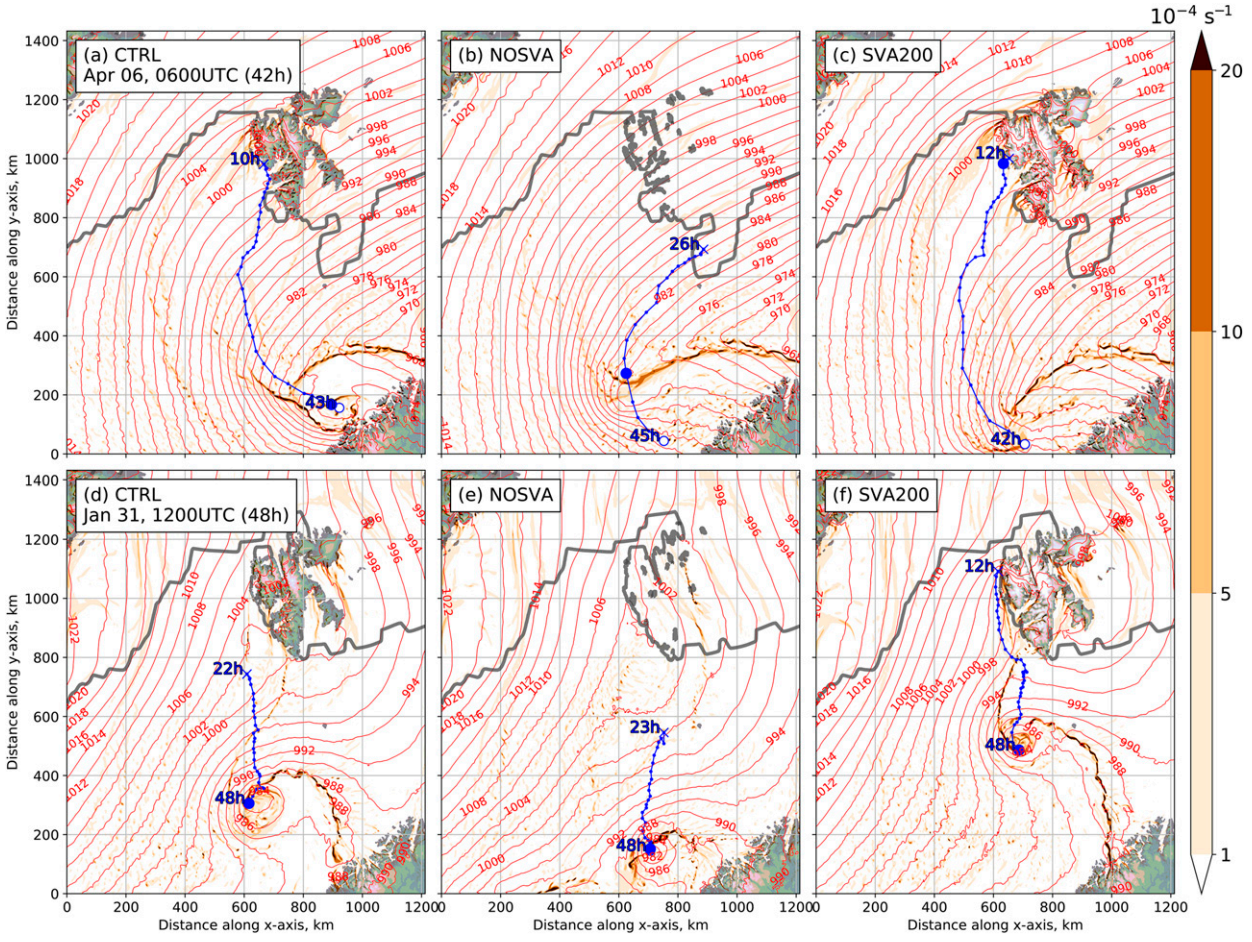

FIG. 7. Results of the sensitivity experiments with changed orography at the time of maximum intensity in the control run. Relative vorticity at 950 hPa (color shading, 10^{-4} s^{-1}) and SLP (red contours, every 2 hPa) in (a),(d) CTRL; (b),(e) NOSVA; and (c),(f) SVA200 simulations of (top) STARS-72 and (bottom) STARS-77. Model elevation is shown in color shading, and sea ice edge is shown by the gray line. Manually tracked PL positions are shown by blue dots. The blue filled circle shows the location of maximum intensity of the PLs. The blue cross shows the beginning of the track and the white circle shows the PL location after 48 h.

its vorticity maximum after about half a day of development while it is less than 200 km away from Svalbard (blue circle in Fig. 7c). Note this allows us to start PL tracking earlier (e.g., by 10 h in STARS-77 case), which is reflected by a longer time series of averaged vorticity (Fig. 8).

2) PERTURBED SEA ICE EXPERIMENTS

In the experiments with increased sea ice cover to the south (ICE76N), the vorticity maxima forming near Svalbard receive a smaller flux of energy from the ice-covered surface, and so are much weaker than in the CTRL runs (Figs. 8, 9).

In the STARS-72 case, the incipient vortex gradually weakens while traveling over the sea ice. Once the cold stably stratified air embedded within the vortex enters the ice-free area south of 76°N, the average sensible heat flux around the vortex center spikes to almost 350 W m^{-2} (Fig. 8c)—comparable to other PLs with high heat fluxes (e.g., Wagner et al. 2011). However, even this boost in surface heating is not enough for the incipient vorticity maximum to evolve into a PL, and instead it disintegrates into convective disturbances that eventually make landfall in northern Norway. The mesoscale SLP trough deepens nonetheless, and the low-level vorticity field is characterized by the strong shear line originating from the rear part of the large-scale low over the Barents Sea (Fig. 9b).

In the STARS-77 case (Fig. 9e), despite the fact that in this simulation the mesoscale vortices develop in the same spot as in the CTRL run, they appear as a series of small-scale shear waves without a dominant center (the SLP minimum is around 4 hPa weaker than the CTRL). The growth of this mesoscale disturbance is hindered by

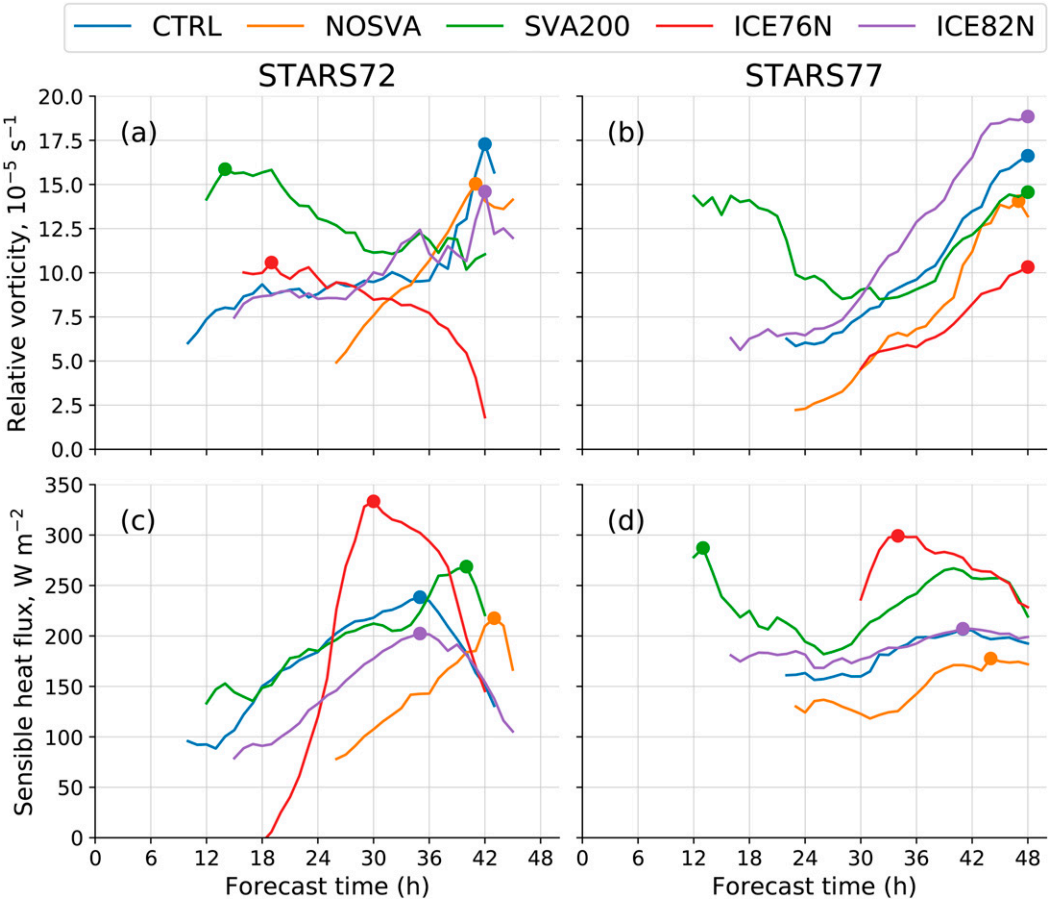

FIG. 8. Time series of (a),(b) average relative vorticity between 950 and 850 hPa and (c),(d) average sensible heat flux within 150-km radius from PL centers for (a),(c) the STARS-72 case and (b),(d) the STARS-77 case, and for each of the sensitivity experiments. The colored circles show the maximum values of each curve.

the lack of surface heat fluxes. Similarly to the NOSVA run, the link to Svalbard is very weak, and it is only due to the vorticity source at the synoptic low periphery that the mesoscale vortices develop at all.

In the retreated sea ice conditions (ICE82N), both PLs undergo a life cycle similar to that of the CTRL run and exhibit almost the same vorticity pattern and development. In the STARS-72 case, the mesoscale cyclone is comparable to the CTRL run when expressed in vorticity (Fig. 8a), surface wind speed, or precipitation rate, although the maximum value of averaged vorticity is slightly smaller than in CTRL. A possible explanation is that the sensible heat flux is also lower during the early stages of the PL life cycle, though not as low as in the ICE76N case. In the STARS-77 case the mesoscale cyclone is slightly stronger in the ICE82N run compared to CTRL, based on the mean low-level vorticity (Fig. 8b) and precipitation rate. However, even though the sensible heat flux is lower during the PL intensification in the ICE82N run (Fig. 8d), the resulting decrease in the vorticity is small. On the other hand, in the STARS-77 case, the vorticity increase appears quite large, compared to the small increase in sensible heat flux early in the life cycle (Fig. 8d).

In short, the impact of replacing the ocean surface with sea ice in the area west of Svalbard (ICE76N) has a greater effect on the intensity of these PLs than changing the sea ice distribution to the north of it (ICE82N).

4. Discussion

In these two cases the primary influence of Svalbard is that it blocks the propagation of a CAO: in experiments with flattened elevation, mesoscale cyclones still form but they are more readily swept away by the northerly flow, while a doubled elevation deflects the cyclone track (as in the STARS-72 case) or slows it down (STARS-77).

A useful metric for assessing the flow response to orographic obstacles is the nondimensional mountain height:

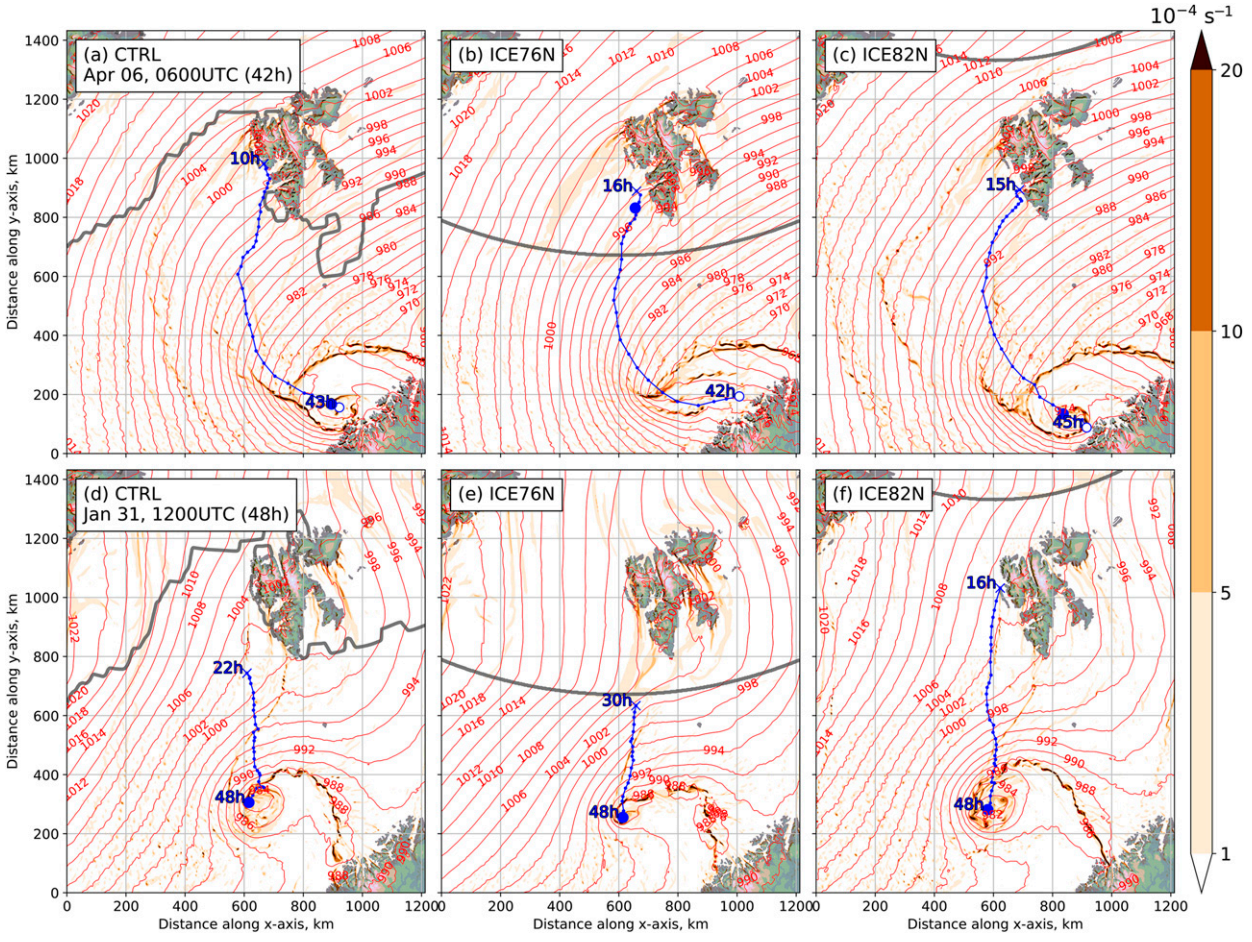

FIG. 9. As in Fig. 7, but for (a),(d) CTRL; (b),(e) ICE76N; and (c),(f) ICE82N sensitivity runs of the (top) STARS-72 and (bottom) STARS-77 cases.

$\hat{h} = Nh/U$. The real atmospheric flow around complex topography is characterized by large variations in the wind speed U and the Brunt–Väisälä frequency N, making it nontrivial to calculate the average $\hat{h}$ (Ólafsson and Bougeault 1997). Following estimates of the nondimensional height in real cases with flow splitting (Ólafsson and Bougeault 1997, and references therein), we obtain N and U in the layer below the mountain-top level and average them separately (rather than averaging their ratio N/U). This calculation is performed for the CTRL experiment of both PL cases using the model output linearly interpolated to 12 equally spaced height levels below 1200 m. The latter is chosen as the mountain-top level h, being roughly equal to the altitude of the highest peak of Svalbard as represented in the MetUM's surface elevation field, and similar to 916 m in a study by Skeie and Gronas (2000). The area used for horizontal averaging is located upwind of the archipelago (Fig. 10c), approximately at a distance equal to the Rossby radius of deformation (Elvidge et al. 2015), $\lambda_R = Nh/f$ (where f is the Coriolis parameter).

The time series of U and N (Figs. 10a,b) demonstrate that the upstream conditions are characterized by stable stratification, with values of N close to ones used by Skeie and Gronas (2000) in their idealized experiments. The average wind velocity is quite low in the first 12–18 h of the STARS-72 case simulation (Fig. 10a), resulting in $\hat{h}$ up to ≈5. Gradually, the wind speed in the lower troposphere increases, due to the strengthening of the large-scale pressure gradient (e.g., see Figs. 2b,c), while N remains constant. Consequently, $\hat{h}$ diminishes, but nevertheless remains larger than unity. In the STARS-77 case (Fig. 10b), even though U is relatively high, the static stability is large too, so $\hat{h}$ stays larger than ≈2 throughout the simulation and increases toward the end. Interestingly, several hours before the formation of the STARS-77 PL, there is a noticeable rise in $\hat{h}$, which may hint at the causality between flow splitting and mesoscale cyclone generation downstream.

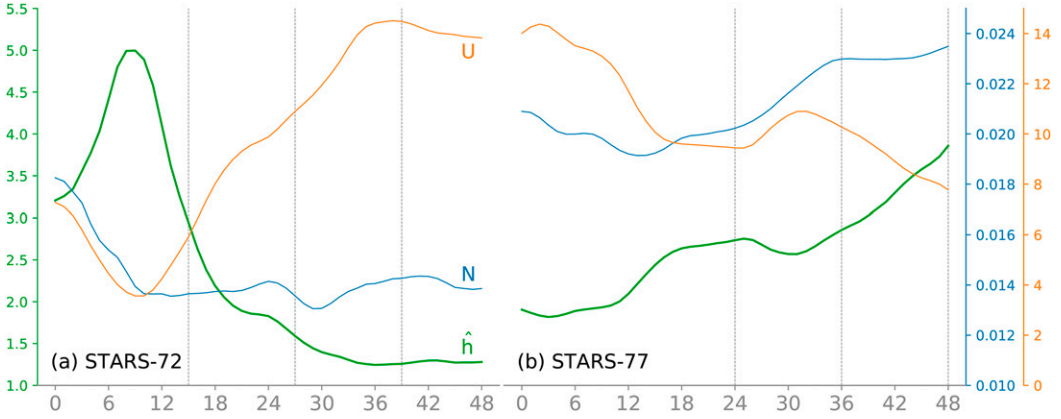

FIG. 10. Time series of the nondimensional height $\hat{h}$, wind speed U ($m\,s^{-1}$), and the Brunt–Väisälä frequency N (s^{-1}) in (a) STARS-72 case and (b) STARS-77 case. Note the vertical lines correspond to the three time slices shown in Figs. 1–3.

These estimates of the nondimensional mountain height indicate that in both cases the atmospheric flow is incapable of climbing the orographic barrier of Svalbard and thus a flow splitting regime is favored. Flow splitting is somewhat visible in the wind speed vectors in Fig. 3, while the wake convergence is also demonstrated by the pattern of backward trajectories (Fig. 5e). As demonstrated theoretically by Smith (1989b) and numerically by Skeie and Gronas (2000), blocking in experiments with realistic orography is more pronounced than in experiments with an idealized mountain, and this can be attributed to the cross-flow-oriented mountain ridges of north Spitsbergen. The sufficient nondimensional height of Svalbard in our cases offers a comparison, for example, with the Sikhote-Alin mountain range, which blocks Siberian cold air masses from the Sea of Japan and creates favorable conditions for mesoscale cyclogenesis (Watanabe et al. 2017).

Under conditions of stable stratification and weak winds, flow splitting leads to wake effects such as eddy shedding, which is manifested by PV anomalies on the flanks of an orographic obstacle (Schär and Smith 1993a; Smith 1989a; Petersen et al. 2003). The presence of these PV anomalies renders the flow susceptible to barotropic instabilities, as was previously demonstrated by idealized experiments with a circular obstacle (e.g., Schär and Smith 1993b). This process of low-level vorticity production is likely to be the case in the two PL cases presented here.

Svalbard's isolated shape and orientation also make it a source of vorticity filaments, which merge into and reinforce vortices downstream. Removing Svalbard, the STARS-72 PL instead grows on the vorticity clusters coming from the Barents Sea, and the STARS-77 PL lacks a vorticity "tail" stretching away from Svalbard. Hence, at least for the mesoscale cyclones similar to STARS-72 and -77, Svalbard plays the role of a secondary vorticity source, albeit not a necessary one for PL intensification.

As for the main vorticity clusters, they form in the rear part of the large-scale cyclone independent of surface conditions near Svalbard (in both PL cases). This southern cluster of vorticity in the central Norwegian Sea emerges at about 23–26 h and intensifies into a shear line. The growth of the shear line is coincident with a high precipitation rate (not shown). This suggests that the latent heat released in the lower troposphere through condensation contributes to PL growth via strong updrafts leading to the stretching of vertical vorticity.

One phenomenological difference between STARS-72 and STARS-77 is the presence of an upper-level PV anomaly. This is illustrated in the SVA200 runs, in which even with higher Svalbard the STARS-72 PL stays on a similar course. The positive PV anomaly is indeed a salient synoptic feature of PL development in cases similar to STARS-72 and is manifested as a short-wave trough in the upper troposphere. Note the shape and magnitude of the upper-level PV filament is very similar to the PV anomaly associated with a Kara Sea PL, analyzed by Verezemskaya and Stepanenko (2016). To test whether the upper-level PV anomaly is strong enough to interact with the low-level mesoscale vortices appearing in the CTRL simulation of the STARS-72 case, we calculate the Rossby penetration depth (Adakudlu and Barstad 2011), which can be approximated by

$$\delta z \approx \frac{L\sqrt{f(f+\zeta_\theta)}}{N},$$

where L is the horizontal scale of the PV anomaly and ζ_θ is the isentropic relative vorticity. At the time of

vigorous PL development (at 1500 UTC 5 April 2007; Fig. 2b), the PV reaches almost 5 PVU (1 PVU = 10^{-6} K kg^{-1} m^2 s^{-1}) and is located close to the 285-K isentropic surface. As can be seen in Figs. 2b and 11, the horizontal scale of the anomaly is roughly 200 km. The relative vorticity ($\zeta_{\theta=285\text{K}}$) contribution to the PV anomaly on this level is about 2.5×10^{-4} s^{-1}, or $\approx 1.8f$, and $N = 0.0092$ s^{-1} in the tropospheric column around the PL center. Using these values, we obtain a Rossby penetration depth of $\approx$4.8 km, which exceeds the vertical distance between the low-level and upper-level PV anomalies. This suggests that one of the mechanisms of the PL development is a dynamical coupling between the low-level disturbance and the upper-level trough.

In the STARS-77 environment, even though the average Brunt–Väisälä frequency is of the same magnitude, the PV field does not have a distinct positive anomaly in the upper troposphere, nor does isentropic relative vorticity, so a dynamical coupling does not appear to be occurring.

One might expect that with a weakened temperature stratification in the ICE82N experiment of the STARS-72 case, the vertical PV coupling would be stronger and lead to a more intense PL. However, as seen from Fig. 8a, the mesoscale cyclone in the STARS-72 case appears slightly weaker compared to the CTRL run. A possible explanation is that in the run with reduced sea ice, the surface heat fluxes are persistently lower, because the convective boundary layer of the northerly flow is more well mixed, reducing the air–sea temperature difference. In ICE76N the presence of sea ice implies that vortices spawned by Svalbard's orography do not gain sufficient strength and dissipate or make landfall.

The cumulative effect of surface fluxes on both PLs is evident from the comparison of the areas under the curves in Figs. 8c and 8d. Even though the total area integrated for the CTRL and ICE76N curves is similar, the heat flux at the beginning of the PL's life cycles is significantly lower in ICE76N than in CTRL. Hence, even though the PLs' development depends on a mix of barotropic and baroclinic processes, surface heat fluxes are still important in their early stages. It appears that in the STARS-72 case, surface fluxes are more important in the very beginning of the PL development than later on.

5. Summary and conclusions

We have carried out numerical simulations of two Norwegian Sea PLs, in which the orography of Svalbard and the sea ice around it were modified to test their role in mesoscale cyclone formation and development. Our focus is on the Norwegian and Barents Seas area, but these results have implications for PL dynamics more

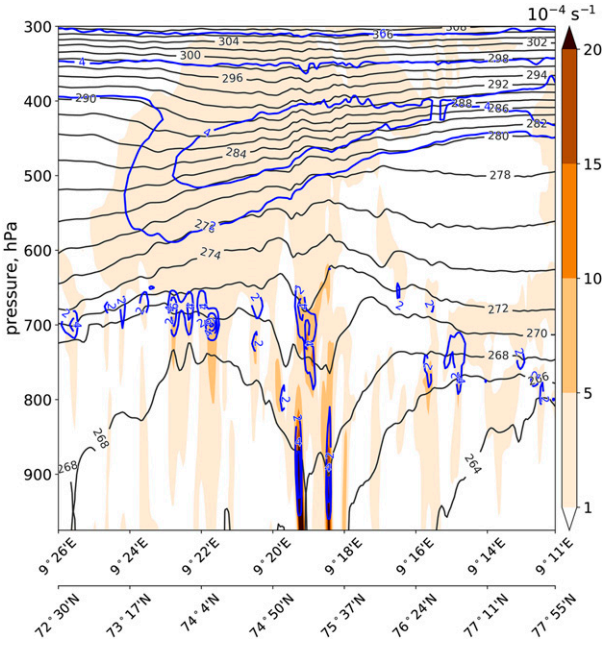

FIG. 11. South–north vertical cross section of relative vorticity (color shading, 10^{-4} s^{-1}), potential temperature (black contours, every 1 K), and potential vorticity (blue contours, every 2 PVU) at 1500 UTC 5 Apr 2007 in the CTRL simulation of the STARS-72 case. The location of the cross section is given in Fig. 2b.

generally. We use a state-of-the-art convection-permitting NWP model that allows for a detailed examination of PL life cycles in the control experiments and how their tracks and intensity change in perturbed scenarios.

Because of a large nondimensional mountain height, Svalbard splits the northerly CAO and produces low-level vorticity filaments that grow to mesoscale cyclones with the help of surface heat fluxes. In the synoptic conditions characterized by the large-scale depression over northern Norway and an anticyclone over Greenland, vorticity filaments emanating from Svalbard need to merge with their counterparts coming from the Barents Sea to form intense PLs, as seen here for both the STARS-72 and STARS-77 cases. In other words, the primary sources are convectively driven convergence lines, while Svalbard's mountains provide a secondary source of vorticity (Fig. 12a). Increasing Svalbard's orography leads to greater vorticity production in the early stages of PL development, as well as deflection of PL tracks. In cases with a prominent upper-level PV anomaly (such as STARS-72) the PL is steered by the cold trough aloft and is less affected by the topographic forcing.

The removal of sea ice to the east of Svalbard and in the Fram Strait results in a moderate intensification of the more convectively driven PL (STARS-77). On the other hand, extending the sea ice cover to the south

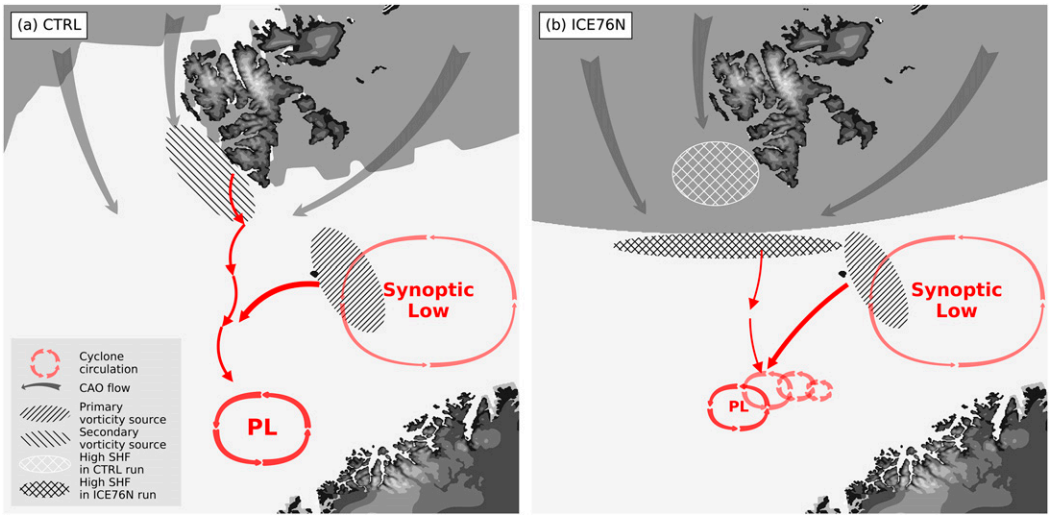

FIG. 12. Schematic representation of mesoscale cyclone generation typical for cases like STARS-72 and STARS-77. Dark gray arrows depict CAO flow curving around Svalbard. The primary source of vorticity for these PLs is on the northwestern periphery of a synoptic-scale cyclone, while the secondary source is located to the west of Svalbard (shown by hatching). The movement of vorticity clusters and their merger into a PL is shown by red arrows. (a) The CTRL simulation. (b) The ICE76N experiment with the sea ice extended to the south, which shows an area with strong sensible heat flux (SHF, cross hatched), which is a (delayed) source of energy for the development of the weaker PLs (shown by smaller red circulations). The high sensible heat flux area in the CTRL experiment is shown in (b) by white cross hatching.

(Fig. 12b) deprives the mesoscale vortices of a necessary heat supply, halting their intensification (STARS-72) or slowing it down (STARS-77). PL development is hindered in this situation, because weaker surface fluxes (see Figs. 8c,d) lead to a more stable stratification and less condensational heating.

The two cases analyzed in our study exemplify that PLs in the northeast Atlantic often begin their evolution from sporadic vorticity filaments and clusters associated with convective cells. Vorticity clusters form in surges at the western part of large-scale depressions, and some of them intensify to PLs with gale-force winds. These two mesoscale cyclones withstand large perturbations to their ambient environment and still develop to sufficient intensity to be labeled as PLs. Thus, we demonstrate that both Svalbard's orography and surrounding sea ice have an impact on the cyclogenesis in the Norwegian Sea to the point of *modulating* it, but not being a dominant factor.

A next step would be to extend our study to more PL cases and examine if these results are robust for different synoptic situations. Compiling a climatology of mesoscale vortices in the vicinity of Svalbard would allow for broader conclusions about the statistically significant influence of orography and sea ice on PL genesis. For example, correlating the nondimensional mountain height upstream of Svalbard and PL formation in the Norwegian Sea.

Acknowledgments. We are thankful to A. Orr and S. Webster for technical assistance with the MetUM. We greatly appreciated the help of M. Sprenger in setting up the LAGRANTO model. We acknowledge use of the MONSooN system, a collaborative facility supplied under the Joint Weather and Climate Research Programme, a strategic partnership between the Met Office and the Natural Environment Research Council. This work was made possible by funding provided by the Natural Environment Research Council under Grant NE/I028297/1 (ACCACIA). The first author was supported by a Lord Zuckerman scholarship at the School of Environmental Sciences, University of East Anglia, and the first two authors benefited from a Bjerknes's visiting fellowship to the University of Bergen in 2017. We thank the three reviewers for their constructive comments.

REFERENCES

Adakudlu, M., and I. Barstad, 2011: Impacts of the ice-cover and sea-surface temperature on a polar low over the Nordic seas: A numerical case study. *Quart. J. Roy. Meteor. Soc.*, **137**, 1716–1730, https://doi.org/10.1002/qj.856.

Albright, M. D., R. J. Reed, and D. W. Ovens, 1995: Origin and structure of a numerically simulated polar low over Hudson Bay. *Tellus*, **47**, 834–848, https://doi.org/10.1034/j.1600-0870.1995.00123.x.

Bracegirdle, T. J., and S. L. Gray, 2008: An objective climatology of the dynamical forcing of polar lows in the Nordic seas. *Int. J. Climatol.*, **28**, 1903–191, https://doi.org/10.1002/joc.1686.

——, and ——, 2009: The dynamics of a polar low assessed using potential vorticity inversion. *Quart. J. Roy. Meteor. Soc.*, **135**, 880–893, https://doi.org/10.1002/qj.411.

Brown, A. R., R. J. Beare, J. M. Edwards, A. P. Lock, S. J. Keogh, S. F. Milton, and D. N. Walters, 2008: Upgrades to the boundary-layer scheme in the Met Office numerical weather prediction model. *Bound.-Layer Meteor.*, **128**, 117–132, https://doi.org/10.1007/s10546-008-9275-0.

Cavalieri, D. J., and C. L. Parkinson, 2012: Arctic sea ice variability and trends, 1979-2010. *Cryosphere*, **6**, 881–889, https://doi.org/10.5194/tc-6-881-2012.

Condron, A., G. R. Bigg, and I. A. Renfrew, 2006: Polar mesoscale cyclones in the northeast Atlantic: Comparing climatologies from ERA-40 and satellite imagery. *Mon. Wea. Rev.*, **134**, 1518–1533, https://doi.org/10.1175/MWR3136.1.

Dacre, H. F., and S. L. Gray, 2006: Life-cycle simulations of shallow frontal waves and the impact of deformation strain. *Quart. J. Roy. Meteor. Soc.*, **132**, 2171–2190, https://doi.org/10.1256/qj.05.238.

Doyle, J. D., and M. A. Shapiro, 1999: Flow response to large-scale topography: The Greenland tip jet. *Tellus*, **51**, 728–748, https://doi.org/10.3402/tellusa.v51i5.14471.

Dritschel, D. G., P. H. Haynes, M. N. Juckes, and T. G. Shepherd, 1991: The stability of a two-dimensional vorticity filament under uniform strain. *J. Fluid Mech.*, **230**, 647–665, https://doi.org/10.1017/S0022112091000915.

Elvidge, A. D., I. A. Renfrew, J. C. King, A. Orr, T. A. Lachlan-Cope, M. Weeks, and S. L. Gray, 2015: Foehn jets over the Larsen C Ice Shelf, Antarctica. *Quart. J. Roy. Meteor. Soc.*, **141**, 698–713, https://doi.org/10.1002/qj.2382.

Gallée, H., 1995: Simulation of the mesocyclonic activity in the Ross Sea, Antarctica. *Mon. Wea. Rev.*, **123**, 2051–2069, https://doi.org/10.1175/1520-0493(1995)123<2051:SOTMAI>2.0.CO;2.

Gryschka, M., C. Drüe, D. Etling, and S. Raasch, 2008: On the influence of sea-ice inhomogeneities onto roll convection in cold-air outbreaks. *Geophys. Res. Lett.*, **35**, L23804, https://doi.org/10.1029/2008GL035845.

Harold, J. M., G. R. Bigg, and J. Turner, 1999: Mesocyclone activity over the Northeast Atlantic. Part 2: An investigation of causal mechanisms. *Int. J. Climatol.*, **19**, 1283–1299, https://doi.org/10.1002/(SICI)1097-0088(199910)19:12<1283::AID-JOC420>3.0.CO;2-T.

Heinemann, G., 1997: Idealized simulations of the Antarctic katabatic wind system with a three-dimensional mesoscale model. *J. Geophys. Res.*, **102**, 13 825–13 834, https://doi.org/10.1029/97JD00457.

Irvine, E. A., S. L. Gray, and J. Methven, 2011: Targeted observations of a polar low in the Norwegian Sea. *Quart. J. Roy. Meteor. Soc.*, **137**, 1688–1699, https://doi.org/10.1002/qj.914.

Joly, A., and A. J. Thorpe, 1990: Frontal instability generated by tropospheric potential vorticity anomalies. *Quart. J. Roy. Meteor. Soc.*, **116**, 525–560, https://doi.org/10.1002/qj.49711649302.

Klein, T., and G. Heinemann, 2002: Interaction of katabatic winds and mesocyclones near the eastern coast of Greenland. *Meteor. Appl.*, **9**, 407–422, https://doi.org/10.1017/S1350482702004036.

Kolstad, E. W., 2006: A new climatology of favourable conditions for reverse-shear polar lows. *Tellus*, **58A**, 344–354, https://doi.org/10.1111/j.1600-0870.2006.00171.x.

——, 2011: A global climatology of favourable conditions for polar lows. *Quart. J. Roy. Meteor. Soc.*, **137**, 1749–1761, https://doi.org/10.1002/qj.888.

Kristjánsson, J. E., S. Thorsteinsson, E. W. Kolstad, and A.-M. Blechschmidt, 2011: Orographic influence of east Greenland on a polar low over the Denmark Strait. *Quart. J. Roy. Meteor. Soc.*, **137**, 1773–1789, https://doi.org/10.1002/qj.831.

Mallet, P.-E., C. Claud, C. Cassou, G. Noer, and K. Kodera, 2013: Polar lows over the Nordic and Labrador Seas: Synoptic circulation patterns and associations with North Atlantic-Europe wintertime weather regimes. *J. Geophys. Res.*, **118**, 2455–2472, https://doi.org/10.1002/jgrd.50246.

Met Office, 2016: Iris: A Python library for analysing and visualising meteorological and oceanographic data sets. Accessed 15 June 2018, https://scitools.org.uk/.

Michel, C., A. Terpstra, and T. Spengler, 2018: Polar mesoscale cyclone climatology for the Nordic Seas based on ERA-Interim. *J. Climate*, **31**, 2511–2532, https://doi.org/10.1175/JCLI-D-16-0890.1.

Montgomery, M. T., and B. F. Farrell, 1992: Polar low dynamics. *J. Atmos. Sci.*, **49**, 2484–2505, https://doi.org/10.1175/1520-0469(1992)049<2484:PLD>2.0.CO;2.

Moore, G. W. K., and I. A. Renfrew, 2005: Tip jets and barrier winds: A QuikSCAT climatology of high wind speed events around Greenland. *J. Climate*, **18**, 3713–3725, https://doi.org/10.1175/JCLI3455.1.

Ólafsson, H., and P. Bougeault, 1997: The effect of rotation and surface friction on orographic drag. *J. Atmos. Sci.*, **54**, 193–210, https://doi.org/10.1175/1520-0469(1997)054<0193:TEORAS>2.0.CO;2.

Outten, S. D., I. A. Renfrew, and G. N. Petersen, 2009: An easterly tip jet off Cape Farewell, Greenland. II: Simulations and dynamics. *Quart. J. Roy. Meteor. Soc.*, **135**, 1934–1949, https://doi.org/10.1002/qj.531.

Papritz, L., and T. Spengler, 2017: A Lagrangian climatology of wintertime cold air outbreaks in the Irminger and Nordic Seas and their role in shaping air–sea heat fluxes. *J. Climate*, **30**, 2717–2737, https://doi.org/10.1175/JCLI-D-16-0605.1.

Petersen, G. N., H. Ólafsson, and J. E. Kristjánsson, 2003: Flow in the lee of idealized mountains and Greenland. *J. Atmos. Sci.*, **60**, 2183–2195, https://doi.org/10.1175/1520-0469(2003)060<2183:FITLOI>2.0.CO;2.

Rasmussen, E., 1981: An investigation of a polar low with a spiral cloud structure. *J. Atmos. Sci.*, **38**, 1785–1792, https://doi.org/10.1175/1520-0469(1981)038<1785:AIOAPL>2.0.CO;2.

——, and J. Turner, Eds., 2003: *Polar Lows: Mesoscale Weather Systems in the Polar Regions.* Cambridge University Press, 630 pp.

Reeve, M. A., and E. W. Kolstad, 2011: The Spitsbergen South Cape tip jet. *Quart. J. Roy. Meteor. Soc.*, **137**, 1739–1748, https://doi.org/10.1002/qj.876.

Renfrew, I. A., S. D. Outten, and G. W. K. Moore, 2009: An easterly tip jet off Cape Farewell, Greenland. I: Aircraft observations. *Quart. J. Roy. Meteor. Soc.*, **135**, 1919–1933, https://doi.org/10.1002/qj.513.

Romero, R., and K. Emanuel, 2017: Climate change and hurricane-like extratropical cyclones: Projections for North Atlantic polar lows and medicanes based on CMIP5 models. *J. Climate*, **30**, 279–299, https://doi.org/10.1175/JCLI-D-16-0255.1.

Schär, C., and H. C. Davies, 1990: An instability of mature cold fronts. *J. Atmos. Sci.*, **47**, 929–950, https://doi.org/10.1175/1520-0469(1990)047<0929:AIOMCF>2.0.CO;2.

——, and R. B. Smith, 1993a: Shallow-water flow past isolated topography. Part I: Vorticity production and wake formation. *J. Atmos. Sci.*, **50**, 1373–1400, https://doi.org/10.1175/1520-0469(1993)050<1373:SWFPIT>2.0.CO;2.

——, and ——, 1993b: Shallow-water flow past isolated topography. Part II: Transition to vortex shedding. *J. Atmos. Sci.*, **50**, 1401–1412, https://doi.org/10.1175/1520-0469(1993)050<1401:SWFPIT>2.0.CO;2.

Sergeev, D. E., I. A. Renfrew, T. Spengler, and S. R. Dorling, 2017: Structure of a shear-line polar low. *Quart. J. Roy. Meteor. Soc.*, **143**, 12–26, https://doi.org/10.1002/qj.2911.

Skeie, P., and S. Gronas, 2000: Strongly stratified easterly flows across Spitsbergen. *Tellus*, **52A**, 473–486, https://doi.org/10.3402/tellusa.v52i5.12281.

Smith, R. B., 1989a: Hydrostatic airflow over mountains. *Advances in Geophysics*, Vol. 31, Academic Press, 1–41, https://doi.org/10.1016/S0065-2687(08)60052-7.

——, 1989b: Mountain-induced stagnation points in hydrostatic flow. *Tellus*, **41A**, 270–274, https://doi.org/10.1111/j.1600-0870.1989.tb00381.x.

Sprenger, M., and H. Wernli, 2015: The LAGRANTO Lagrangian analysis tool – version 2.0. *Geosci. Model Dev.*, **8**, 2569–2586, https://doi.org/10.5194/gmd-8-2569-2015.

Verezemskaya, P. S., and V. M. Stepanenko, 2016: Numerical simulation of the structure and evolution of a polar mesocyclone over the Kara Sea. Part 1. Model validation and estimation of instability mechanisms. *Russ. Meteor. Hydrol.*, **41**, 425–434, https://doi.org/10.3103/S1068373916060078.

Wagner, J. S., A. Gohm, A. Dörnbrack, and A. Schäfler, 2011: The mesoscale structure of a polar low: Airborne lidar measurements and simulations. *Quart. J. Roy. Meteor. Soc.*, **137**, 1516–1531, https://doi.org/10.1002/qj.857.

Walters, D., and Coauthors, 2017: The Met Office Unified Model Global Atmosphere 6.0/6.1 and JULES Global Land 6.0/6.1 configurations. *Geosci. Model Dev.*, **10**, 1487–1520, https://doi.org/10.5194/gmd-10-1487-2017.

Watanabe, S.-I., and H. Niino, 2014: Genesis and development mechanisms of a polar mesocyclone over the Japan Sea. *Mon. Wea. Rev.*, **142**, 2248–2270, https://doi.org/10.1175/MWR-D-13-00226.1.

——, ——, and W. Yanase, 2017: Structure and environment of polar mesocyclones over the northeastern part of the Sea of Japan. *Mon. Wea. Rev.*, **145**, 2217–2233, https://doi.org/10.1175/MWR-D-16-0342.1.

——, ——, and ——, 2018: Composite analysis of polar mesocyclones over the western part of the Sea of Japan. *Mon. Wea. Rev.*, **146**, 985–1004, https://doi.org/10.1175/MWR-D-17-0107.1.

Webster, S., A. R. Brown, D. R. Cameron, C. Jones, and C. P. Jones, 2003: Improvements to the representation of orography in the Met Office Unified Model. *Quart. J. Roy. Meteor. Soc.*, **129**, 1989–2010, https://doi.org/10.1256/qj.02.133.

Wood, N., and Coauthors, 2014: An inherently mass-conserving semi-implicit semi-Lagrangian discretization of the deep-atmosphere global non-hydrostatic equations. *Quart. J. Roy. Meteor. Soc.*, **140**, 1505–1520, https://doi.org/10.1002/qj.2235.

Zahn, M., and H. Von Storch, 2010: Decreased frequency of North Atlantic polar lows associated with future climate warming. *Nature*, **467**, 309–312, https://doi.org/10.1038/nature09388.